



Few-layered-graphene/zirconia composites: Single-step powder synthesis, spark plasma sintering, microstructure and properties

Andréas Flaureau, Alicia Weibel, Geoffroy Chevallier, Jérôme Esvan,
Christophe Laurent, Claude Estournès

► To cite this version:

Andréas Flaureau, Alicia Weibel, Geoffroy Chevallier, Jérôme Esvan, Christophe Laurent, et al.. Few-layered-graphene/zirconia composites: Single-step powder synthesis, spark plasma sintering, microstructure and properties. Journal of the European Ceramic Society, 2022, 42 (5), pp.2349-2361. 10.1016/j.jeurceramsoc.2022.01.006 . hal-03601450

HAL Id: hal-03601450

<https://hal.science/hal-03601450>

Submitted on 8 Mar 2022

HAL is a multi-disciplinary open access archive for the deposit and dissemination of scientific research documents, whether they are published or not. The documents may come from teaching and research institutions in France or abroad, or from public or private research centers.

L'archive ouverte pluridisciplinaire **HAL**, est destinée au dépôt et à la diffusion de documents scientifiques de niveau recherche, publiés ou non, émanant des établissements d'enseignement et de recherche français ou étrangers, des laboratoires publics ou privés.









Open Archive Toulouse Archive Ouverte (OATAO)

OATAO is an open access repository that collects the work of Toulouse researchers and makes it freely available over the web where possible

This is an author's version published in: <http://oatao.univ-toulouse.fr/28895>

Official URL: <https://doi.org/10.1016/j.jeurceramsoc.2022.01.006>

To cite this version:

Flaureau, Andréas  and Weibel, Alicia  and Chevallier, Geoffroy  and Esvan, Jérôme  and Laurent, Christophe  and Estournès, Claude  *Few-layered-graphene/zirconia composites: Single-step powder synthesis, spark plasma sintering, microstructure and properties.* (2022) Journal of the European Ceramic Society, 42 (5). 2349-2361. ISSN 0955-2219

Any correspondence concerning this service should be sent to the repository administrator: tech-oatao@listes-diff.inp-toulouse.fr

Few-layered-graphene/zirconia composites: Single-step powder synthesis, spark plasma sintering, microstructure and properties

Andréas Flaureau^a, Alicia Weibel^a, Geoffroy Chevallier^{a,b}, Jérôme Esvan^c,
Christophe Laurent^a, Claude Estournès^{a,*}

^a CIRIMAT, CNRS-INP-UPS, Université Toulouse 3 Paul Sabatier, Université Toulouse 3 - Paul Sabatier, 118 route de Narbonne, 31062, Toulouse cedex 9, France

^b Plateforme Nationale CNRS de Frittage Flash, PNP², Université Toulouse 3 Paul Sabatier, 118 route de Narbonne, 31062, Toulouse cedex 9, France

^c CIRIMAT, CNRS-INP-UPS, INP-ENSLACET, 4 allée Emile Monso, BP 44362, 31030, Toulouse cedex 4, France

ARTICLE INFO

Keywords:

Few-layered-graphene

Zirconia

CVD

Nanocomposites

Mechanical and electrical properties

ABSTRACT

The chemical vapor deposition of carbon is performed onto a commercial yttria-stabilized zirconia (3YSZ) powder bed. This produces few-layered-graphene (FLG) film uniformly covering the 3YSZ grains, without the manipulation of any pre-existing nanocarbon in the form of graphene platelets. The powders are then consolidated by spark plasma sintering, producing specimens where FLG is located along the grain boundaries of the 3YSZ matrix, which is below 0.3 μm in grain size. The samples are characterized by Raman spectroscopy, X-ray photoelectron spectroscopy, scanning and transmission electron microscopy. The pure 3YSZ exhibits higher toughness and fracture strength compared to composites, but the trend is that their toughness increases upon the increase in carbon content. Crack-deflection and crack-bridging are observed. The composites are electrically conducting with a percolation threshold between 1.48 and 1.98 vol.% of carbon, reflecting the continuous nature of the FLG film over very long distances.

1. Introduction

The dispersion of graphene into a ceramic matrix may give rise to composites [1–4] with very attractive mechanical and physical properties. The samples are usually prepared by lengthy routes that involve mixing a ceramic powder with agglomerates of more or less defective graphene prepared by graphite exfoliation [5,6], followed by sintering. This produces a microstructure where few-layered-graphene (FLG) platelets of limited lateral dimensions are dispersed as discrete particles in the ceramic matrix. Graphene nanosheets or nano-platelets, which are thicker stacks up to about 100 nm, are also reported. By contrast, a fast, one-step method has been reported where a magnesia [7] or alumina [8, 9] powder bed is submitted to a thermal treatment provoking the decomposition of a carbon-containing gas, resulting in the uniform deposition of FLG films (1–8 layers) covering the ceramic grains. The microstructure after sintering therefore consists in a continuous FLG film located along the grain boundaries, in contrast to samples prepared by the mixing route. Other *in situ* routes have been reported but they are restricted to the particular cases of SiC [10] and other carbides [11]. By contrast, the present one-step method is inherently versatile and we here

propose to apply it to stabilized zirconia powder bed. Zirconia ceramics, notably those stabilized in the tetragonal or cubic phase, show very interesting properties that permit some use in many high-value application fields including biomaterials, aerospace, energy and sensors [12–16]. The FLG/ZrO₂ powders are consolidated by spark plasma sintering (SPS) and their microstructure, mechanical and electrical properties are investigated. The specimens are compared to those prepared by other authors using mixing routes [17–33].

2. Material and methods

2.1. Raw materials

A commercial 3 mol.% Y₂O₃-ZrO₂ powder (Tosoh TZ-3Y-E, 40 nm) was used and denoted 3YSZ in the following. This compound is sold as mostly tetragonal-stabilized zirconia. A chemical vapor deposition (CVD) treatment was performed in order to deposit carbon onto the 3YSZ grains. For each sample, a powder bed (12 g) was heated in Ar (10 L/h) up to 900 °C (15 °C/min). Upon reaching 900 °C, methane (CH₄) was introduced (1, 3, and 4 L/h) while keeping the total gas flow-rate

* Corresponding author.

E-mail address: estournes@chimie.ups-tlse.fr (C. Estournès).

Table 1

Ar/CH₄ atmosphere composition, carbon proportion in weight (C_n) and volume (C_v), volume fraction of monoclinic phase (f_m), calculated density (ρ_{calc}), Raman I_D/I_G ratio, I_{2D}/I_G ratio and 2D band position with their standard deviation, for the samples in powder form.

Specimen	Ar/CH ₄ (L/h)	C _n (wt.%)	C _v (vol.%)	f _m (vol.%)	ρ _{calc} (g. cm ⁻³)	I _D /I _G	I _{2D} /I _G	2D (cm ⁻¹)
3YSZ	–	0	0	23	6.06	–	–	–
G0	10/0	0	0	3	6.12	–	–	–
G148	9/1	0.52	1.48	2	6.07	1.76 ± 0.05	0.45 ± 0.02	2650 ± 3
G198	7/3	0.70	1.98	8	6.03	1.56 ± 0.06	0.48 ± 0.07	2646 ± 2
G252	6/4	0.89	2.52	12	5.99	1.49 ± 0.05	0.43 ± 0.05	2648 ± 3

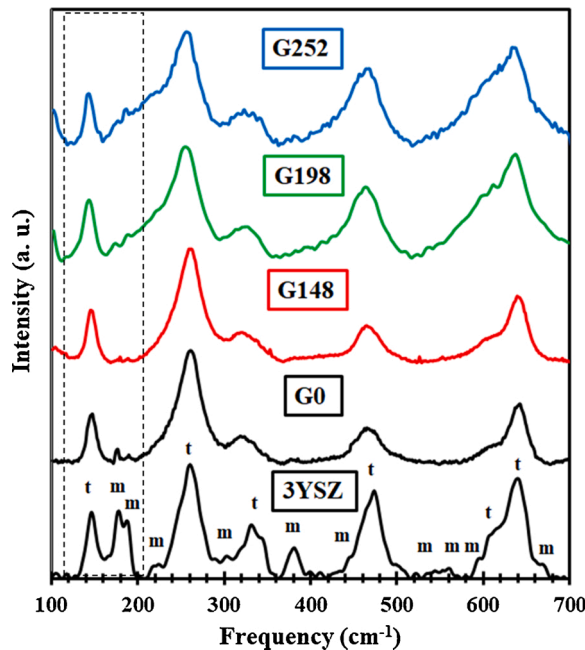


Fig. 1. Low-frequency Raman spectra of the 3YSZ, G0, G148, G198 and G252 powders. The spectra are normalized with the more intense band at 100 %.

constant (10 L/h). The flow-rates are monitored by mass-flow controllers. After a 75 min dwell at 900 °C, cooling down to room temperature was performed in the same Ar/CH₄ atmosphere. A powder bed was treated similarly but without introducing methane, for the sake of comparison with the untreated 3YSZ on the one hand and the other powders on the other hand.

2.2. Sintering

The untreated 3YSZ and the composite powders were consolidated by SPS (Dr Sinter 632LX, Fuji Electronic Industrial Co., Japan) with a direct current (on : off) pulse pattern of (40 ms : 7 ms). About 5.7 g of 3YSZ powder or 4.7 g of composite powder were loaded into a 20 mm inner-diameter graphite die. A graphite foil (PERMA-FOIL®Toyo Tanso) was placed between punches and die and between die and powder for easy removal. Prior to the thermal cycle, a pre-compaction step (50 MPa, 2 min) was performed at room temperature in the SPS cell to ensure that all samples have a similar green state. The temperature was raised up to 600 °C in 3 min and maintained there for 3 min, in order to obtain a homogenous temperature in the entire sample. The temperature is controlled by an optical pyrometer with a 570 °C threshold detection focused on a hole (3 mm deep) at the external surface of the die. The temperature was increased with a heating rate of 100 °C/min to a set-point of 1150 °C and 1450 °C for the 3YSZ and composites powders respectively, where an 11 min dwell was performed. Upon reaching this temperature, a uniaxial pressure was applied in 1 min, equal to 100 and 150 MPa for the 3YSZ and composites powders, respectively. It was maintained for 8 min and then released in 1 or 2 min for the 3YSZ and

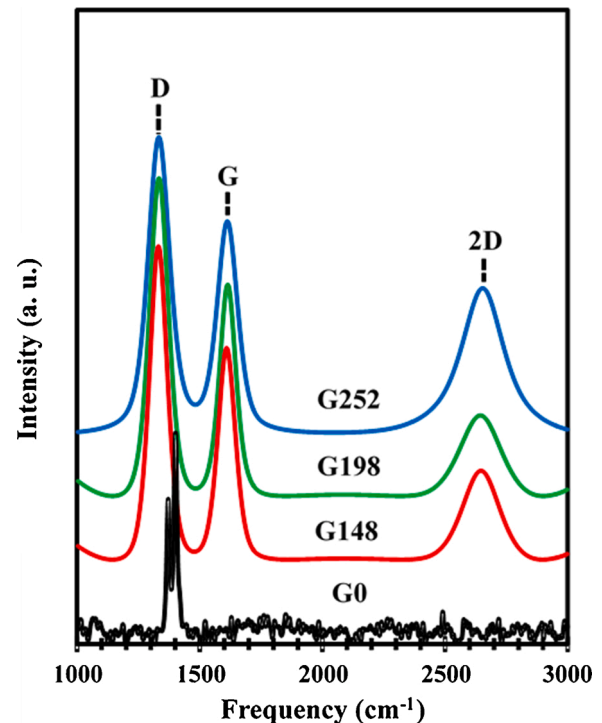


Fig. 2. High-frequency Raman spectra of the G0, G148, G198 and G252 powders. The G0 spectrum is normalized with the more intense band at 100 %. The G148, G198 and G252 spectra are normalized with the G band at 100 %.

composites powders, respectively. After the pressure release, the temperature was decreased down to 600 °C at 60 °C.min⁻¹ and then under natural cooling. For the 3YSZ samples, the residual graphitic foil was removed by a long thermal treatment at 800 °C (4 h heating, 4 h dwell and 4 h cooling). For the composite samples, the residual graphitic foil was removed by polishing. The final samples are about 2 mm thick.

2.3. Characterization

The carbon content in the powders was quantified by means of the flash combustion method (±2 % accuracy). Raman spectra (Confocal microscope RAMAN Labram HR 800 Yvon Jobin) were recorded for the powders, sintered specimens and on the fracture profiles, using a 633 nm laser (each spectrum presented is the average of three spectra). The low-frequency range (100–700 cm⁻¹) was investigated in order to evaluate the proportions of monoclinic and tetragonal zirconia [34,35]. The high-frequency range (1000–3000 cm⁻¹) was investigated in order to detect the presence of graphene and evaluate its structural quality. The X-ray photoelectron emission spectra were recorded using a mono-chromatised Al K_α (hν = 1486.6 eV) source on a Thermo Scientific K-Alpha system. The X-ray spot size was about 400 μm. The pass energy was fixed at 30 eV with a step of 0.1 eV for core levels and at 160 eV for surveys (step 1 eV). The spectrometer energy calibration was done using the Au 4f_{7/2} (83.9 ± 0.1 eV) and Cu 2p_{3/2} (932.8 ± 0.1 eV)

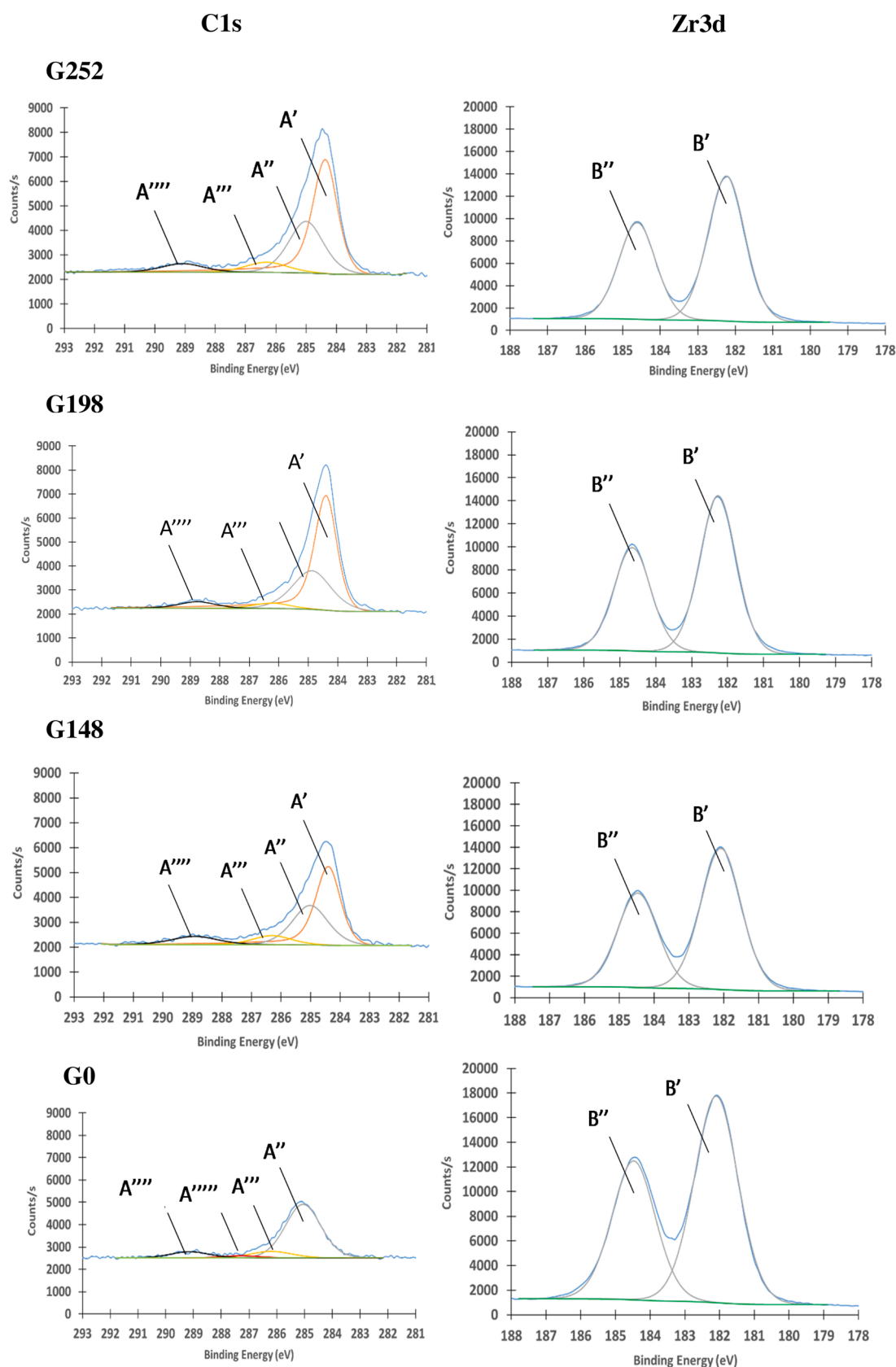


Fig. 3. XPS spectra of the G0, G148, G198 and G252 powders. A': C=C; A'': C-C; C-H; A''': C-O; A'''': O=C-O; A''''': C=O; B': Zr3d_{5/2} Zr-O; B'': Zr3d_{3/2} Zr-O.

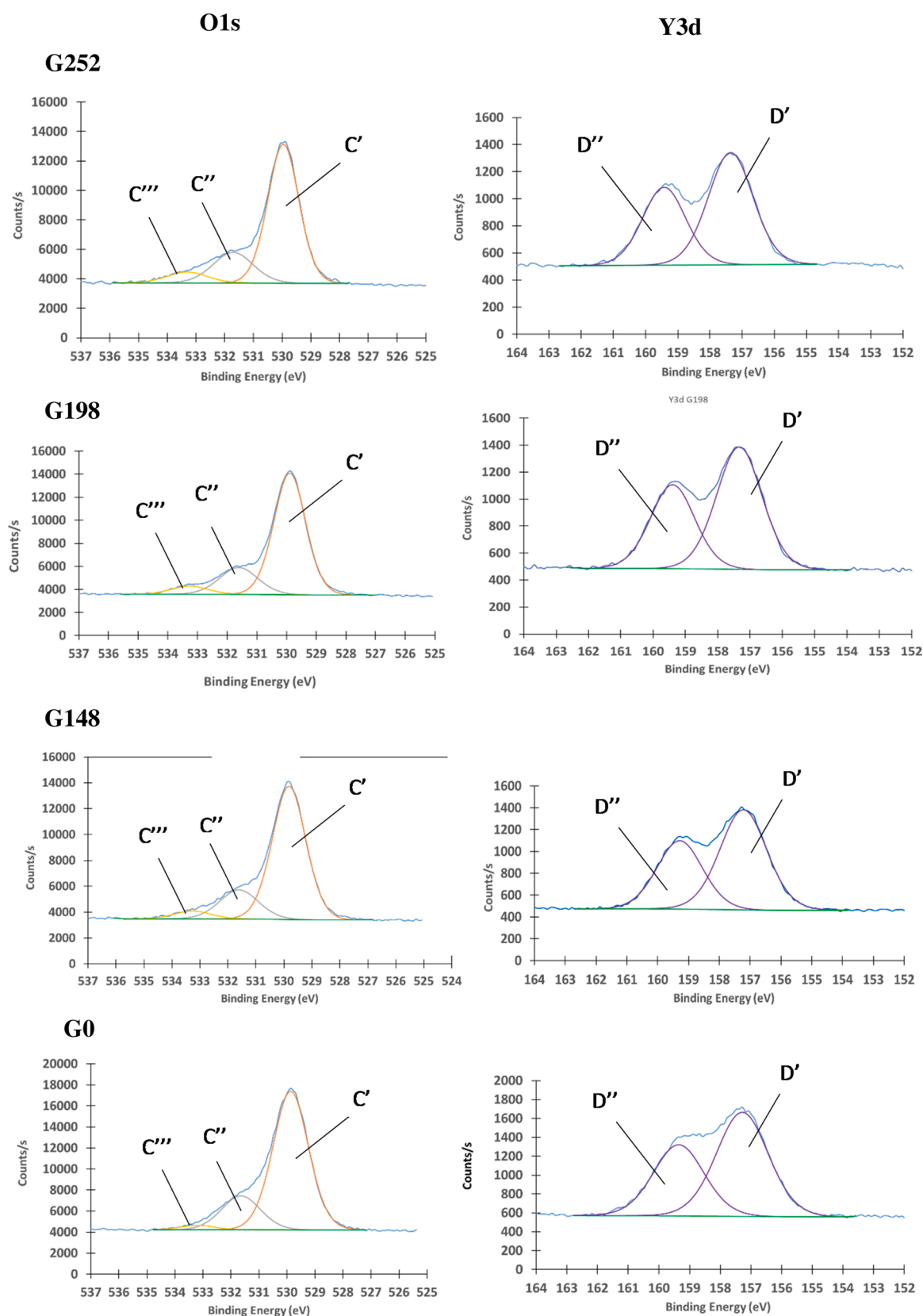


Fig. 4. XPS spectra of the G0, G148, G198 and G252 powders (G148, G198 and G252). C' : Lattice O, oxides; C'' : O Vacancies, CO; C''' : CO; D' : $Y_3d_{5/2}$ Y-O; D'' : $Y_3d_{3/2}$ Y-O.

Table 2

Curve fitting results of the XPS C1s, Zr3d_{5/2}, Zr3d_{3/2}, O1s, Y3d_{5/2} and Y3d_{3/2} spectra of the powders: binding energy (BE), full width at half-maximum (FWHM) and proportion (P).

	G0			G148			G198			G252		
	BE (eV)	FWHM (eV)	P (at. %)	BE (eV)	FWHM (eV)	P (at. %)	BE (eV)	FWHM (eV)	P (at. %)	BE (eV)	FWHM (eV)	P (at. %)
C1s C=C	—	—	—	284.4	1.0	19.6	284.4	0.9	26.8	284.4	1.0	27.2
C1s C—C, C—H	285.1	1.5	17.9	285.0	1.4	12.5	284.9	1.5	13.4	285.0	1.4	15.2
C1s C=O	286.2	1.7	2.5	286.3	1.5	3.2	286.2	1.4	1.8	286.3	1.6	3.6
C1s C=O	287.3	1.6	0.7	—	—	—	—	—	—	—	—	—
C1s O=C—O	289.1	1.6	2.2	288.9	1.8	3.4	288.8	1.4	2.2	289.1	1.6	3.0
Zr3d _{5/2} Zr-O	182.1	1.5	12.9	182.1	1.4	10.1	182.3	1.2	9.0	182.2	1.2	8.2
Zr3d _{3/2} Zr-O	184.5	1.5	8.6	184.5	1.4	6.7	184.7	1.2	6.0	184.6	1.2	5.5
O1s Lattice O oxides	529.9	1.5	40.5	529.8	1.4	32.3	529.9	1.3	29.1	530.0	1.3	25.8
O1s O Vacancies,CO	531.7	1.6	10.9	531.6	1.6	8.2	531.6	1.5	7.7	531.7	1.6	7.3
O1s others CO	533.2	1.5	1.3	533.3	1.5	2.1	533.3	1.4	2.3	533.3	1.6	2.6
Y3d _{5/2} Y-O	157.3	2.0	1.5	157.2	1.8	1.2	157.3	1.7	1.1	157.4	1.7	1.0
Y3d _{3/2} Y-O	159.4	2.0	1.0	159.3	1.7	0.8	159.4	1.6	0.7	159.4	1.6	0.7

photoelectron lines. XPS spectra were recorded in direct mode N (Ec) and the background signal was removed using the Shirley method. The flood gun was used to neutralize charge effects on the top surface. Selected samples were observed by field-emission-gun scanning electron microscopy (FESEM, JEOL JSM 7800 F) and transmission electron microscopy (TEM, JEOL JEM 2100 F). Platinum coating was performed in order to increase the contrast by enhancing secondary electrons emission of carbon. For TEM observations, a thin foil was prepared using a procedure involving grinding with SiC paper, dimpling (GATAN 656) with a 1 µm diamond suspension and cold ion milling at 4 kV (GATAN PIPS 691).

The density of the sintered samples was evaluated using Archimedes' method (hydrostatic balance Sartorius MSE224S-YDK03). The relative density was calculated using 5.817 g.cm⁻³ for m-ZrO₂, 6.134 g.cm⁻³ for t-ZrO₂ and 2.1 g.cm⁻³ for graphene. Indentation tests were performed with a 200 g pressure for 10 s on the polished surface of the specimens by loading with a Vickers microindenter (Mitutoyo HM 2000). The transverse fracture strength (σ_f) was measured, parallel to the SPS pressing axis, by the three-point bending method (Material Testing Systems MTS 1/M) on specimens about 1.8 × 1.8 × 18 mm³ machined with a diamond blade. The span between the two supporting pins is equal to 13 mm. Cross-head speed was fixed at 0.1 mm/min. The toughness (K_{IC}) was evaluated, also parallel to the pressing axis, by the single-edged notched beam (SENB) method on similar specimens notched with a diamond wire 0.17 mm in diameter. The notch depth/sample thickness ratio was verified to be slightly higher than 0.4. A calibration factor was used to calculate the SENB toughness from the experimental results [36]. For the carbon-free (untreated) 3YSZ, 25 samples were tested for σ_f and 23 for K_{IC}. For the composites, five samples were tested for both. The electrical conductivity was measured, using a two points probe, at room temperature with a direct current applied on parallelepipedic specimens (1.8 × 1.8 × 5 mm³), machined from the pellets in directions perpendicular and parallel to the SPS pressing axis, respectively. A silver paste was applied in order to connect the conducting electrodes. The current densities used were lower than 160 mA/cm² (Keithley 2400).

3. Results and discussion

3.1. Powders

The carbon content for the composites prepared using 1, 3 and 4 L/h of CH₄ is equal to 1.48, 1.98 and 2.52 vol.%, respectively (Table 1). For the sake of brevity, these samples will be denoted as G148, G198 and G252 hereafter. The 3YSZ powder prepared without introducing CH₄ contains no carbon and therefore will be denoted as G0. The low-frequency range of the Raman spectra were normalized with the most intense band corresponding to the t-ZrO₂ phase (around 260 cm⁻¹) at 100 % (Fig. 1). The volume fraction of m-ZrO₂ (f_m, Table 1) was

determined from the spectra using Eqs. (1) and (2) [34,35]:

$$x_m = \frac{I_{m(180\text{ cm}^{-1})} + I_{m(192\text{ cm}^{-1})}}{I_{m(180\text{ cm}^{-1})} + I_{m(192\text{ cm}^{-1})} + I_{t(148\text{ cm}^{-1})}} \quad (1)$$

where, I represents the intensity of bands accounting for the monoclinic (m) or tetragonal (t) phases.

$$f_m = \sqrt{0,19 \frac{0,13}{x_m - 1,01}} \quad 0,56 \quad (2)$$

where f_m is the volume fraction of m-ZrO₂ and x_m is the intensity ratio as determined by Eq. (1).

The untreated (commercial) 3YSZ powder contains about 23 vol.% of m-ZrO₂ (f_m - Table 1). For G0, the proportion of m-ZrO₂ is significantly lower (f_m = 3 vol.%). The monoclinic to tetragonal (m → t) phase transformation, normally occurring at 1170 °C, is observed at a lower temperature (900 °C) probably because of the nanometric size of the grains [37]. No significant difference is observed between G148 and G0, while for G198 and G252 powders, an interesting f_m increase is noted upon the increase in carbon content. This could indicate a partial inhibition of the m → t phase transformation by graphene as evidenced [38] for nanometric graphene-pure ZrO₂ composite powders. The density of the powders, calculated using the proportions of m-ZrO₂, t-ZrO₂ and carbon, decreases slightly upon the increase in carbon content (ρ_{calc} - Table 1).

The high-frequency range Raman spectra are shown in Fig. 2. For G0, no band that could correspond to graphene or any carbon species could be detected. The double band at about 1400 cm⁻¹ is characteristic of Al₂O₃ [39], which is the main impurity in the sample (0.253 wt.%, as given by the supplier).

The Raman spectra of the composite powders show the D, G and 2D bands characteristic of carbon at about 1330 cm⁻¹, 1606 cm⁻¹ and 2650 cm⁻¹, respectively. The spectra were normalized with the G band at 100 %. The Al₂O₃ bands are no more detected on these spectra, probably because they are masked by the intense D band. The I_D/I_G ratio decreases and the I_{2D}/I_G ratio is constant (Table 1) upon the increase in carbon content, which could reflect fewer defects in the graphene layers and a more or less constant number of layers, respectively [40]. The I_D/I_G values are higher than those found for graphene grown by CVD on metallic substrates because of several factors contributing to increase I_D (sp³ like carbon): i) this is FLG, not pristine single-layer graphene, and thus more defects are present; ii) the FLG film is curved, not flat, because the "substrate" is a powder bed constituted of 3YSZ grains 40 nm in diameter; iii) these grains are locally faceted, which could provoke the formation of defects (kinks) in the deposited FLG and thus increase the proportion of defects. The I_{2D}/I_G ratio and the position of the 2D band do not change (Table 1) upon the increase in carbon content, which could indicate that the number of graphene layers is not markedly different

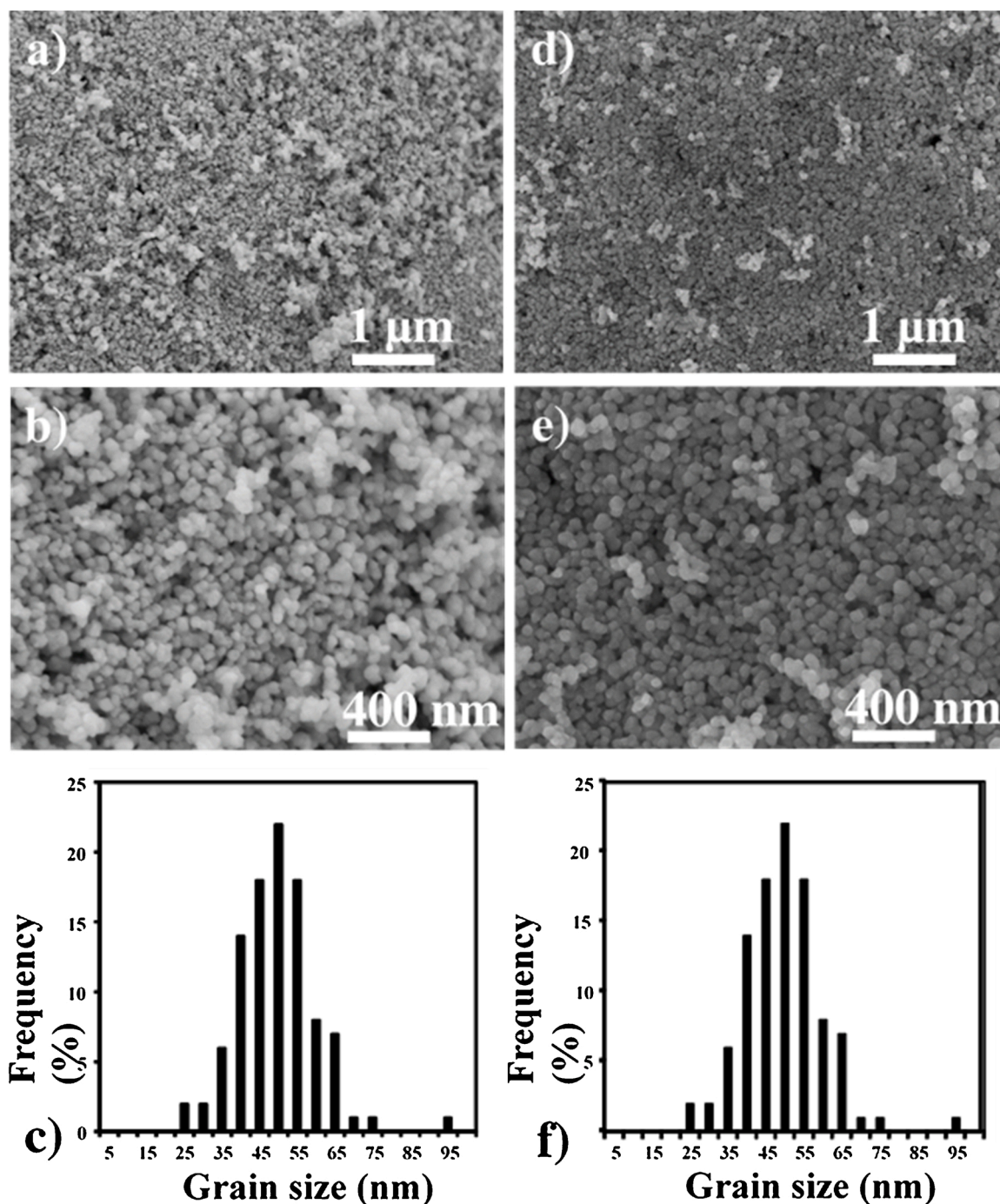


Fig. 5. FESEM images of the G0 (a, b) and G252 (c, d) powders. Grain size distribution for G0 (e) and for G252 (f).

from one sample to the other. The position and shape of the 2D band are in agreement with values commonly observed for FLG with less than 5 layers [41–43].

The XPS spectra are presented in Figs. 3 and 4. A graphene sample prepared in-house was used as a reference for carbon environments. The semi-quantification of each chemical group contribution is reported in Table 2. The range 280–290 eV shows the response of carbon C1s (Fig. 3). The different C1s contributions in the spectra are denoted by A symbols: A': 284.4 eV for C=C, A'': 285 eV for C—C, C—H, A''': 286.2 eV for C—O, A''': 287.0–288 eV for C=O and A''': near 289 eV for O=C—O. The C1s signals for G148, G198 and G252 are similar to each other and show an asymmetrical carbon at low binding energy (A') highlighting the presence of graphene (sp^2 carbon hybridization).

Hydrocarbon (A''), C—O (A''') and carbonyl/ester groups (A'''' and A''''') contributions are detected too.

The C1s response for G0 comes from atmospheric pollution. No zirconium carbides (C-Zr, C1s contributions < 283 eV) neither zirconium oxycarbides (C-Zr-O-C) were detected. The 180–185 eV range describes the presence of zirconium Zr3d (Fig. 3). For all samples, the values at 182.1–182.3 eV (B' component) and 184.5–184.6 eV (B'' component) indicate mainly that the Zr^{4+} environment is similar to the one in pure zirconia. The O1s (Fig. 4) gives three components, an oxide response at 529.8–530 eV (C') corresponding to O-Zr and O-Y, another at 531.6–531.7 eV (C'') for oxygen vacancies, organics (CO) and at 533.2–533.3 eV (C''') for others organics (CO). The values at 157.2–157.4 eV (component D') and 159.3–159.4 eV (component D'')

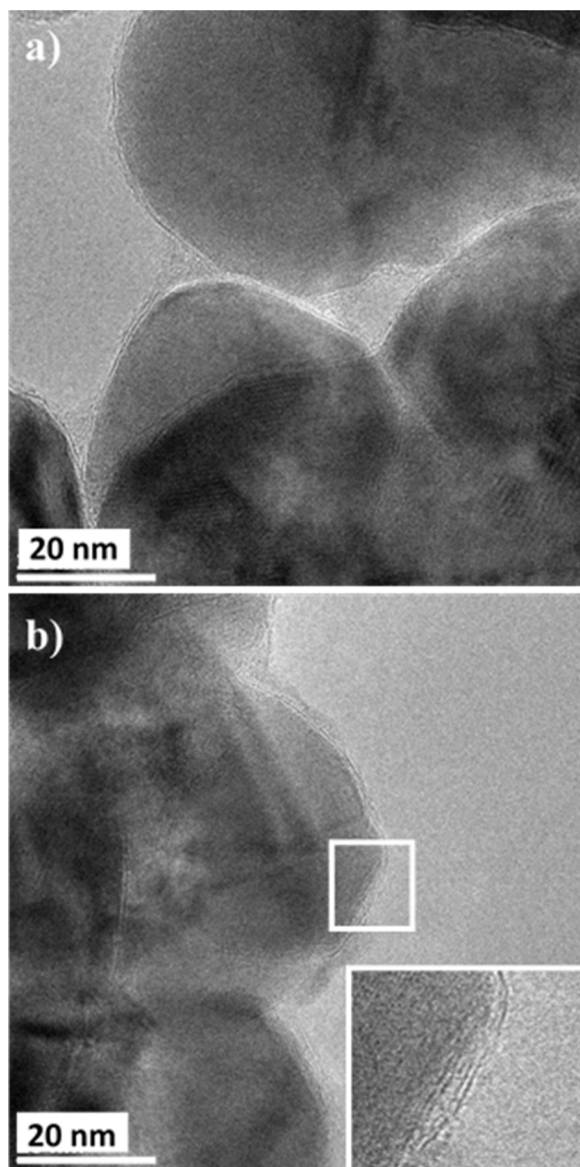


Fig. 6. TEM images of the G148 powder. Insert: graphene layers at zirconia grain surface.

show mainly the presence of yttrium oxide (Y^{3+} form) (Fig. 4).

Typical FESEM images for G0 (Fig. 5a, b) show non-agglomerated grains. The size distribution (Fig. 5c), as deduced from the measurement of hundreds of grains on such images, is in the range 25–75 nm, with an average size equal to 47 ± 11 nm. For G252, the images (Fig. 5d, e) and size distribution (Fig. 5f) are similar. No graphene film is observed at these magnifications. Typical TEM images for G148 (Fig. 6) reveal the presence of 2–4 graphene layers uniformly wrapping the 3YSZ grains. It is possible that the disordered carbon that may be observed, although rarely, results from some degradation under the electron beam.

3.2. Dense samples

The Raman spectra of the sintered samples in the low-frequency range are shown in Fig. 7. 3YSZ and G148 present only the peaks characteristic of the tetragonal phase, indicating that all the monoclinic phase present in the corresponding powders (Table 1) transformed into the tetragonal one during sintering which is performed at temperatures equal or higher than 1150 °C. For G198 and G252, the volume fractions of monoclinic phase (Table 3) are similar to those determined on the

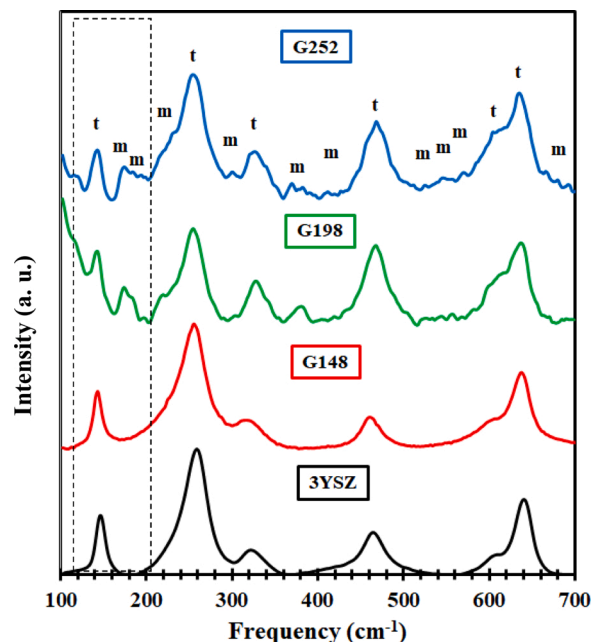


Fig. 7. Low-frequency Raman spectra recorded on the surface of the 3YSZ, G148, G198 and G252 samples after sintering. The spectra are normalized with the more intense band at 100 %.

Table 3

Ar/CH₄ atmosphere composition, carbon content (C_n - wt.%, C_v - vol.%), volume fraction of monoclinic phase (f_m) and Raman I_D/I_G ratio, I_{2D}/I_G ratio and 2D band position with their standard deviation, for the samples after densification by SPS.

Specimen	Ar/ CH ₄ (L/h)	C_n (wt. %)	C_v (vol. %)	f_m (vol. %)	I_D/I_G	I_{2D}/I_G	2D (cm ⁻¹)
3YSZ	10/0	0	0	0	–	–	–
G148	9/1	0.52	1.48	0	1.44 ± 0.04	0.52 ± 0.04	2650 ± 3
G198	7/3	0.70	1.98	9	1.75 ± 0.10	0.44 ± 0.05	2650 ± 3
G252	6/4	0.89	2.52	12	1.50 ± 0.07	0.49 ± 0.09	2650 ± 3

corresponding powders (Table 1). As observed for the powders, graphene inhibits the $m \rightarrow t$ phase transformation for a volume content around 2 vol.% as already reported [29]. This also shows that no $t \rightarrow m$ transformation occurs during cooling from the maximum SPS temperature. The Raman spectra of the sintered samples in the high-frequency range are shown in Fig. 8. For 3YSZ, the spectrum is fairly noisy, which makes the interpretation difficult but, as for the corresponding powder, the more intense bands around 1400 and 1600 cm⁻¹ are characteristic of alumina impurities. Both the I_D/I_G and I_{2D}/I_G ratio as well as the 2D band position (Table 3) are close to those found for the corresponding powders (Table 1), which could indicate that no or little damage occurred to the graphene films during SPS.

The relative density (d - Table 4) is equal to 99 % for 3YSZ and slightly decreases upon the increase in carbon content, reaching 97 % for G252. The average grain size (g - Table 4) was calculated from measurements on low-magnification FESEM images of fracture profiles (Fig. 9). The average zirconia grain size was determined from such images by the mean linear intercept method described by Mendelson [44]. The average grain size is equal to 0.20 ± 0.06 μ m for 3YSZ (Fig. 9a), which was sintered at 1150 °C, as mentioned above. It is similar for G148 (Fig. 9b), 0.20 ± 0.07 μ m, despite a sintering temperature of 1450 °C and is slightly higher upon a further increase in carbon content: 0.25

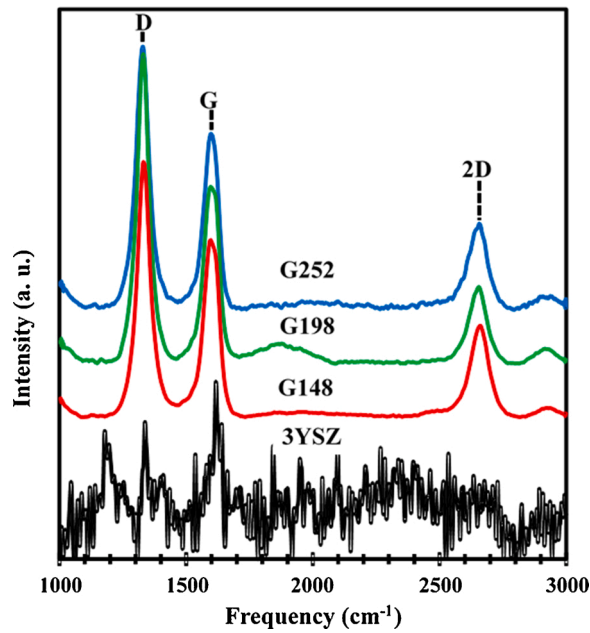


Fig. 8. High-frequency Raman spectra recorded on the surface of the 3YSZ, G148, G198 and G252 samples after sintering. The spectra are normalized with the more intense band at 100 % for G0 and the G band at 100 % for G148, G198 and G252.

Table 4

Characteristics and electrical conductivity of the sintered specimens: carbon content (C_n and C_v), relative density (d), matrix grain size (g), electrical conductivity perpendicular (σ_{\perp}) and parallel (σ_{\parallel}) to the SPS pressing axis.

Specimen or Ref.	C_n (%)	C_v (%)	d (%)	g (μm)	σ_{\perp} (S. cm^{-1})	σ_{\parallel} (S. cm^{-1})
3YSZ	0	0	99	0.20 ± 0.06	–	–
G148	0.52	1.48	99	0.20 ± 0.07	–	–
G198	0.70	1.98	98	0.25 ± 0.08	0.69	0.19
G252	0.89	2.52	97	0.29 ± 0.10	0.98	0.23
[19]	0	0	100	0.29	–	–
	1.7	4.4	99	0.21	0.38	0.14
	3.7	9.5	100	0.25	1.11	0.16
[20]	3.5	9.0	100	0.25	1.13	0.17
	3.7	9.4	98	0.22	1.24	1.25
	3.6*	9.2	96	0.18	4.71	4.06
[21]	1.7	4.4	99	–	0.45	0.13
	3.7	9.5	100	–	1.13	0.17
	10	23.4	100	–	2.76	2.34
[26]	0	–	95	0.142	–	–
	1	–	96	0.130	0.09	–
	3	–	95	0.096	0.98	–
[30]	2	–	–	–	–	2.80

* This particular sample was prepared by a "dry method" and its characteristics and electrical conductivity are markedly different from the other samples in the report [20].

$\pm 0.08 \mu\text{m}$ and $0.29 \pm 0.10 \mu\text{m}$ for G198 (Fig. 9c) and G252 (Fig. 9d), respectively. These results could reflect that the graphene film surrounding the 3YSZ grains strongly limits the movement of the grain boundaries and thus hampers grain growth while for the same powder in similar conditions grains sizes higher than 400 nm were observed in the absence of graphene [35]. Moreover, the uniform grain size for the composites could reflect the homogeneous dispersion of graphene at the 3YSZ grain boundaries and hence the homogeneous dispersion of the FLG films around the 3YSZ powder grains. The fracture is intergranular with some transgranular zones occasionally observed for 3YSZ and G148. FESEM images also reveal partly debonded FLG films (arrowed in Fig. 9). HRTEM images of a thin foil of G252 (Fig. 10) show fringes

corresponding to fairly well-organized FLG, about $5\text{--}10 \text{ nm}$ thick, located at the grain boundaries. Locally, about $4\text{--}30$ graphene layers could be observed.

No electrical conductivity could be measured for 3YSZ and G148 (Table 4), whatever the direction of measurement is perpendicular (σ_{\perp}) or parallel (σ_{\parallel}) to the pressing axis. For G198 and G252, σ_{\perp} is about four times higher than σ_{\parallel} . A similar behavior has already been observed for FLG-magnesia [7] and FLG-alumina [9] samples prepared by the same method, reflecting an anisotropy which would have originated either from the alignment of some of the FLG and/or defects in some areas of FLG both induced by a uniaxial pressing effect during the SPS densification of the composites". Indeed, when the granular body is densified by SPS, the friction between the grains along the z -axis, corresponding to the direction of application of the load, is probably higher than that between the grains in the x - y plane. As a result, tearing off of some FLG may occurred and/or defects can be created on FLG along the z -axis, which may alter their electrical conductivity and consequently induces anisotropy of the electrical properties of the samples. Unfortunately, the presence of such defects cannot be evidenced experimentally. The maximum value for σ_{\perp} is 0.98 S. cm^{-1} for G252. Values only slightly higher (1.1 S. cm^{-1}) are reported for composites with a much higher carbon content ($9\text{--}10 \text{ vol.}\%$) [19–21]. This could reflect the difference in microstructure, either a continuous FLG film over long distances in the present specimens as opposed to discrete submicron-sized FLG platelets.

This could also account for the value of the electrical percolation threshold : between 1.48 and $1.98 \text{ vol.}\%$ of carbon with the present continuous FLG film, lower than what was reported (between 2.2 and $4.4 \text{ vol.}\%$) for FLG-platelets containing samples [19]. Percolation thresholds below $1 \text{ vol.}\%$ were reported for carbon nanotube - oxide composites [45–47], including 3YSZ-matrix composites [48,49], because the carbon nanotubes, with a very high length/diameter ratio and being much longer than the matrix grains, offer a very large connectivity and provide a conducting path in the insulating matrix. Also, it is worth noting that by contrast to the present results, it has been reported [50] that the existence of an interconnected, or close to interconnected, network of carbon nanotubes at the 3YSZ grain boundaries, as evidenced by a measurable electrical conductivity, seems to be the key point in promoting the $t \rightarrow m$ transformation during the SPS cooling stage because of the lack of enough elastic constraint provided by the neighboring zirconia grains in these areas.

The Vickers microhardness (H_v - Table 5) for 3YSZ is equal to 15.4 GPa . It decreases progressively, reaching 10.6 GPa for G258, upon the increase in carbon content and the corresponding decrease in relative density. This is in line with reports by other researchers (Table 5). The fracture strength (σ_f - Table 5) for 3YSZ is equal to $733 \pm 267 \text{ MPa}$, which is lower than reported values [21,27]. It is almost twice lower for the composites, without much difference between them, which could reflect some weakening of the grain boundaries. The toughness (K_{Ic} - Table 5) for 3YSZ is equal to $15.7 \pm 4.0 \text{ MPa.m}^{1/2}$, which is significantly higher than SENB values reported elsewhere [17, 21–25]. For the composites, the toughness is lower than for 3YSZ, unlike in other reports [17, 21–25]. Several groups have reported [24,26,27,29,31–33] toughness values calculated from indentation cracks, but it has been reported that this method overestimates toughness [51,52], for example for carbon nanotube - ceramic samples [53–55] and carbon nanofiber - zirconia samples [56,57]. SENB [58] and SEVNB [59] techniques are to be preferred, for sub-micron and nanometric ceramics, respectively. Note however that for one report in particular [17], it is fairly difficult to understand how adding only $0.01 \text{ wt.}\%$ of graphene could give a 61% increase in toughness over the unreinforced zirconia, as claimed. Interestingly, for the composites, the toughness tends to increase upon the increase in carbon content, being equal to 4.3 , 4.7 and $6.5 \text{ MPa.m}^{1/2}$ for G148, G198 and G252, respectively. This could be related to the $t \rightarrow m$ transformation during cooling from the SPS maximum temperature and/or to the stress-induced $t \rightarrow m$ transformation. Indeed, it has been

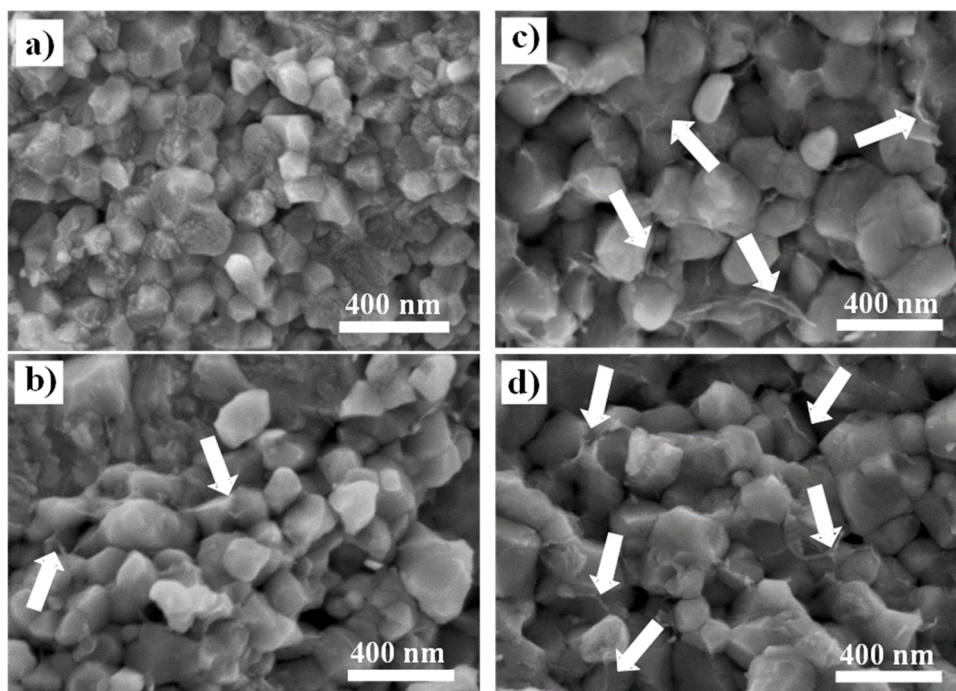


Fig. 9. FESEM images of the 3YSZ (a), G148 (b), G198 (c) and G252 (d) samples after sintering. See text for sintering conditions.

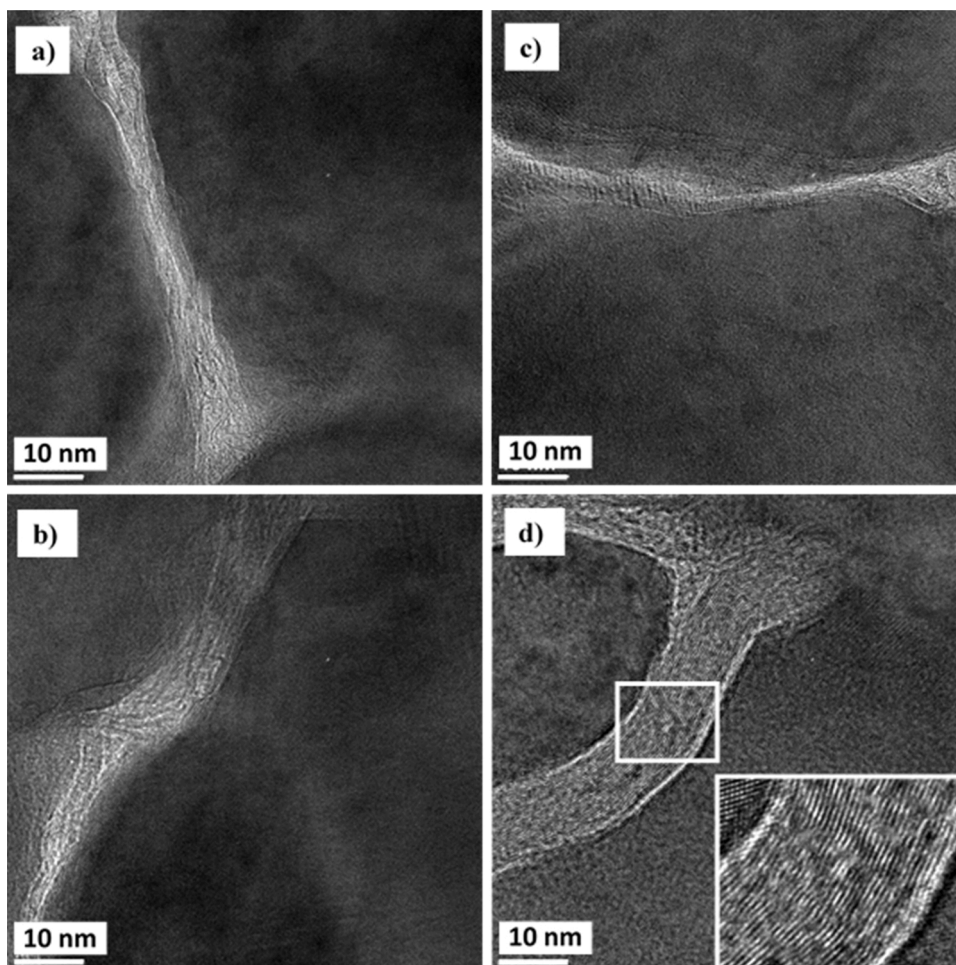


Fig. 10. HRTEM images of the G252 sample after sintering. Insert: graphene layers at grain boundaries.

Table 5

Characteristics and mechanical properties of the sintered specimens: carbon content (C_n and C_v), relative density (d), matrix grain size (g), Vickers micro-hardness ($HV_{0.2}$ for this work but not necessarily for other authors), fracture strength (σ_f), toughness (K_{IC}) from the SENB method or the indentation method (*).

Specimen or Ref.	C_n (%)	C_v (%)	d (%)	g (μm)	$HV_{0.2}$ (GPa)	σ_f (MPa)	K_{IC} (MPa.m ^{1/2})
3YSZ	0	0	99	0.20 ± 0.06	15.4	733 ± 267	15.7 ± 4.0
G148	0.52	1.48	99	0.20 ± 0.07	13.9	393 ± 58	4.3 ± 0.2
G198	0.70	1.98	98	0.25 ± 0.08	11.3	351 ± 33	4.7 ± 0.5
G252	0.89	2.52	97	0.29 ± 0.10	10.6	424 ± 54	6.5 ± 1.6
[17]	0	–	99.2	–	12.5	–	9.5
	0.01	–	99.4	–	12.3	–	15.3
	0.03	–	99.2	–	12.6	–	13.5
	0.05	–	98.9	–	13.0	–	10.5
[19]	0	0	100	0.29	13.9	–	–
	1.7	4.4	99	0.21	11.7	–	–
	3.7	9.5	100	0.25	8.1	–	–
[21]	0	0	99	–	–	1080	7.4
	0.5	3.29	99	–	–	1045	7.7
	1.0	6.41	99	–	–	1000	8.6
	1.5	9.36	99	–	–	975	7.8
[24]	0	0	97.7	0.90	11.0	–	4.1 *
	0.5	2.81	97.5	0.14	12.4	–	5.6 *
	0.8	4.17	96.3	0.13	12.1	–	5.3 *
	1.0	5.49	96.0	0.11	11.7	–	4.7 *
[25]	–	0	99.6	0.385	12.2	–	6.1
	–	0.51	98.3	0.138	13.1	–	6.9
	–	0.76	97.0	0.125	13.5	–	8.0
	–	1.02	96.8	0.103	13.9	–	8.6
	–	1.27	95.6	0.132	12.3	–	8.3
[26]	0	–	95	0.142	–	–	1.5 *
	1	–	96	0.130	–	–	5.1 *
	3	–	95	0.096	–	–	7.0 *
[27]	0	0	99	< 0.5	14.5	1425	4.8 *
	0.4	1.0	99	–	13.0	900	4.9 *
	0.8	2.0	99	1.0	11.5	775	4.9 *
	1.1	3.0	98	> 1.0	9.5	600	4.7 *
	1.5	4.0	97	> 1.0	9.0	525	4.5 *
[29]	0	0	99.1	–	13.6	–	7.8 *
	0.1	0.2	99.2	–	14.4	–	8.1 *
	0.2	0.5	99.1	–	14.5	–	8.5 *
	0.4	1.0	99.1	–	14.6	–	11.0 *
	0.7	2.0	98.0	–	13.3	–	12.8 *
[31]	0	0	87.8	0.15	13.2	–	3.8 ± 0.2 *
	0.1	0.27	88.2	0.15	14.4	–	4.2 ± 0.3 *
	0.2	0.54	90.4	0.19	15.2	–	4.4 ± 0.3 *
	0.5	1.34	89.9	0.17	16.1	–	4.4 ± 0.2 *
	1	2.66	94.2	0.19	16.6	–	4.6 ± 0.3 *
	2	5.23	95.1	0.17	14.9	–	4.5 ± 0.2 *
[32]	0	–	99.6	0.45	12.7	–	6.1 ± 0.6 *
	0.05	–	99.3	0.35	13.4	–	9.0 ± 0.1 *
	0.09	–	99.5	0.30	13.4	–	10.6 ± 0.8 *
	0.2	–	99.3	0.26	13.8	–	8.2 ± 0.9 *
[33]	–	0	99	0.19	13.9	–	3.0 *
	–	1.0	99	0.09	13.8	–	4.0 *
	–	3.0	99	0.08	13.7	–	5.3 *
	–	5.0	99	0.07	13.7	–	6.2 *

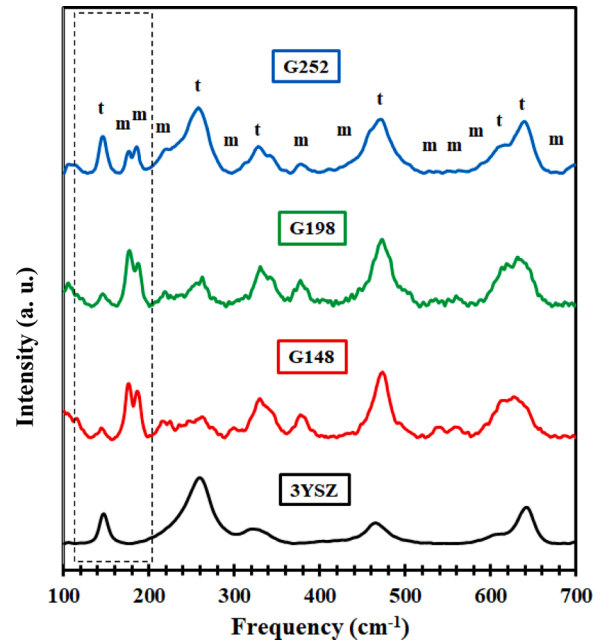


Fig. 11. Low-frequency Raman spectra recorded on the fracture surface of the 3YSZ, G148, G198 and G252 toughness test samples after sintering. The spectra are normalized with the more intense band at 100 %.

Table 6

Relative density (d), volume fraction of monoclinic phase (f_m) as deduced from the Raman spectra in the powders (also in Table 1) on the surface of the sintered samples (also in Table 3) and on the fracture surface and toughness (K_{IC}).

Specimen	d (%)	f_m powder (vol.%)	f_m surface (vol.%)	f_m fracture surface (vol.%)	K_{IC} (MPa.m ^{1/2})
3YSZ	99	23	0	0	15.7 ± 4.0
G148	99	2	0	66	4.3 ± 0.2
G198	98	8	9	57	4.7 ± 0.5
G252	97	12	12	14	6.5 ± 1.6

reported [50] for carbon nanotube - zirconia composites that an increase of K_{IC} should be expected as the $t \rightarrow m$ transformation during cooling is increased upon the increase in the carbon nanotube content at the grain boundaries. However, as noted above, no $t \rightarrow m$ transformation occurs during cooling from the maximum SPS temperature in the present samples. The Raman spectra in the low-frequency range were recorded, for all the sintered samples, on the fracture surface of toughness test samples (Fig. 11). The spectra were compared to those recorded on the surface of the samples (Fig. 7). The volume fraction of monoclinic phase as deduced from the Raman spectra on the surface of the sintered samples and on the fracture surface is reported in Table 6. For 3YSZ, no monoclinic phase is detected for both cases.

The high fracture toughness obtained for 3YSZ sample (obtained on several specimen) is probably a consequence of high densification (99 %), low grain size (< 300 nm) and modified grain boundaries structure due to SPS process. However, this result deserves more work to be fully explained. For G148, there is a very strong difference (0 and 66 vol.%, respectively), which could reflect the presence of graphene, as compared to no graphene at all, favors the stress-induced $t \rightarrow m$ phase transformation. However, upon the increase in graphene content, the extent of transformation becomes lower for G198 (9 and 57 vol.%, respectively) and then insignificant for G252 (12 and 14 vol.%, respectively). Other authors [60] reported a similar trend for carbon nanotube - 3YSZ composites, or no transformation at all [49], but other researchers reported the contrary [50,61]. More local characterizations could be

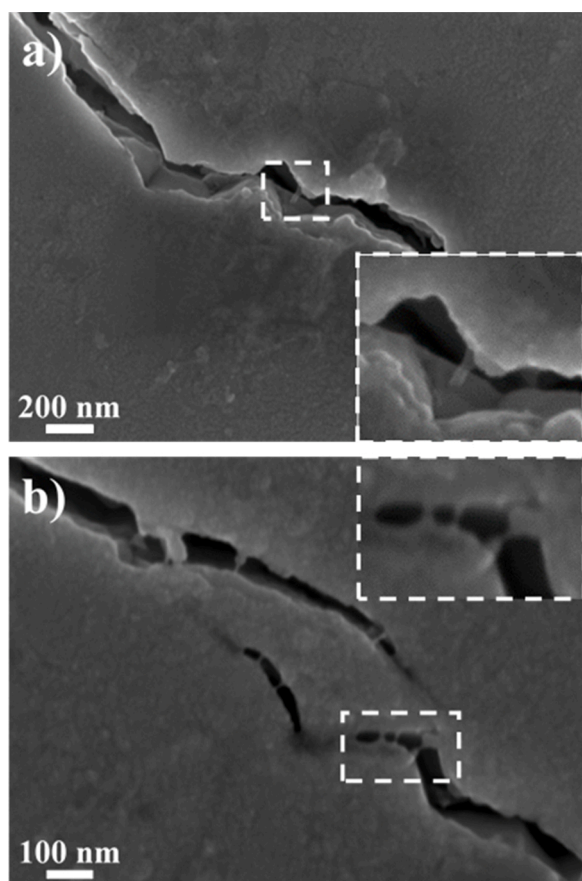


Fig. 12. FESEM images of the G252 sample after sintering, showing cracks generated after high load (2 kg) Vickers indentation. Insert: a) graphene debonding, b) crack-bridging.

useful in order to confirm the absence of any stress-induced $t \rightarrow m$ transformation near the cracks. Note that the observed decrease in stress-induced transformability also reflects the decrease in relative density (d - Table 6). The differences in porosity and $t \rightarrow m$ transformability could account for the differences in toughness but the relationships between these phenomena are too complex [62,63] and need further investigations to be discussed in the present article. High-load (2 kg) Vickers indentations were performed on the polished surface of G252 in order to produce cracks (Fig. 12). The cracks are intergranular and the images reveal crack-deflection, the debonding of the FLG film between two 3YSZ grains (inset in Fig. 12a) and crack-bridging (inset in Fig. 12b). Such reinforcement mechanisms have indeed been reported for different graphene-oxide composites [7–9,17,21,25] and therefore this could account for the moderate toughness increase observed here for the composites upon the increase in graphene content.

4. Conclusion

We have reported the preparation of graphene-3YSZ composite powders by a single-step method using the chemical vapor deposition of carbon onto the grains of a commercial nanometric 3YSZ powder. Therefore, there are no lengthy mixing processes with the possibility of damaging any pre-existing graphite or graphene platelets. The carbon is deposited in the form of few-layered-graphene films around the 3YSZ grains. The samples consolidated by SPS show a moderate decrease of the relative density upon the increase in carbon content. It is shown that a FLG film, as opposed to discrete particles, is located along the grain boundaries of the 3YSZ grains, which are less than 0.3 μm in size. The high connectivity of the electrically conducting graphene allow some

composite samples to be conducting, the percolation threshold being between 1.48 and 1.98 vol.% of carbon. The untreated, carbon-free 3YSZ sample is hard (15.4 GPa), strong (733 MPa) and very tough (15.7 $\text{MPa}\cdot\text{m}^{1/2}$). The so-obtained composites exhibit lower mechanical properties than pure 3YSZ, however it is clearly shown that between them, the trend is that the toughness increases (from 4.3 to 6.5 $\text{MPa}\cdot\text{m}^{1/2}$) upon the increase in carbon content (from 1.48 to 2.52 vol.%). It is shown that this could be due to a combination of the differences in relative density and increasing inhibition of the stress-induced $t \rightarrow m$ transformation, which warrant further studies. Moreover, intergranular crack-deflection, crack-bridging and the debonding of the FLG film between two 3YSZ grains have been observed, which could reflect a direct reinforcing role of the graphene film. Finally, it seems reasonable to think that the reinforcement of a zirconia matrix is all the more difficult when its toughness is already very high, because the presence of the FLG film could be detrimental to the involved reinforcement mechanisms. Therefore work is in progress to apply this method to cubic-zirconia samples, which are known to show a very low toughness in addition to interesting electronic- and ionic-conductivity properties.

Data availability

Data will be made available on request.

Declaration of Competing Interest

None.

Acknowledgments

Electron microscopy was performed at "Centre de micro-caractérisation Raimond Castaing – UAR 3623" (Toulouse) and the authors thank L. Weingarten for help with the TEM observations. The SPS was performed at the Plateforme Nationale CNRS de Frittage-Flash (PNF², Toulouse). Authors would like to thank Adam Berrais for his help in the Raman study of the materials

References

- [1] H. Porwal, S. Grasso, M.J. Reece, Review of graphene–ceramic matrix composites, *Adv. Appl. Ceram.* 112 (2013) 443–454, <https://doi.org/10.1179/174367613X13764308970581>.
- [2] A. Nieto, A. Bisht, D. Lahiri, C. Zhang, A. Agarwal, Graphene reinforced metal and ceramic matrix composites: a review, *Int. Mater. Rev.* 62 (2017) 241–302, <https://doi.org/10.1080/09506608.2016.1219481>.
- [3] P. Miranzo, M. Belmonte, M.I. Osendi, From bulk to cellular structures: a review on ceramic/graphene filler composites, *J. Eur. Ceram. Soc.* 37 (2017) 3649–3672, <https://doi.org/10.1016/j.jeurceramsoc.2017.03.016>.
- [4] K. Markandan, J.K. Chin, M.T.T. Tan, Recent progress in graphene based ceramic composites: a review, *J. Mater. Res.* 32 (2017) 84–106, <https://doi.org/10.1557/jmr.2016.390>.
- [5] W.S. Hummers, R.E. Offeman, Preparation of graphitic oxide, *J. Am. Chem. Soc.* 80 (1958) 1339, <https://doi.org/10.1021/ja01539a017>.
- [6] M. Yi, Z. Shen, A review on mechanical exfoliation for the scalable production of graphene, *J. Mater. Chem. A* 3 (2015) 11700–11715, <https://doi.org/10.1039/C5TA00252D>.
- [7] A. Weibel, D. Mesguich, G. Chevallier, E. Flahaut, Ch. Laurent, Fast and easy preparation of few-layered-graphene/magnesia powders for strong, hard and electrically conducting composites, *Carbon* 136 (2018) 270–279, <https://doi.org/10.1016/j.carbon.2018.04.085>.
- [8] M. Hrubovčáková, E. Múdra, R. Bureš, A. Kovalčíková, R. Sedlák, V. Gírmán, P. Hvizdůš, Microstructure, fracture behaviour and mechanical properties of conductive alumina-based composites manufactured by SPS from graphenated Al_2O_3 powders, *J. Eur. Ceram. Soc.* 40 (2020) 4818–4824, <https://doi.org/10.1016/j.jeurceramsoc.2020.03.072>.
- [9] A. Weibel, A. Flautre, A. Pham, G. Chevallier, J. Esvan, C. Estournès, C. Laurent, One-step synthesis of few-layered-graphene/alumina powders for strong and tough composites with high electrical conductivity, *J. Eur. Ceram. Soc.* 40 (2020) 5779–5789, <https://doi.org/10.1016/j.jeurceramsoc.2020.06.029>.
- [10] P. Miranzo, C. Ramírez, B. Román-Manso, L. Garzón, Humberto R. Gutiérrez, M. Terrones, C. Ocal, M.I. Osendi, M. Belmonte, In situ processing of electrically conducting graphene/SiC nanocomposites, *J. Eur. Ceram. Soc.* 33 (2013) 1665–1674, <https://doi.org/10.1016/j.jeurceramsoc.2013.01.021>.

- [11] M. Naguib, Y. Gogotsi, Synthesis of two-dimensional materials by selective extraction, *Acc. Chem. Res.* 48 (2015) 128–135, <https://doi.org/10.1021/ar500346b>.
- [12] B. Basu, Toughening of yttria-stabilised tetragonal zirconia ceramics, *Int. Mater. Rev.* 50 (2005) 239–256, <https://doi.org/10.1179/174328005X41113>.
- [13] L.B. Chen, Yttria-stabilized zirconia thermal barrier coatings - a review, *Surf. Rev. Lett.* 13 (2006) 535–544, <https://doi.org/10.1142/S0218625X06008670>.
- [14] J. Chevalier, What future for zirconia as a biomaterial? *Biomaterials* 27 (2006) 535–543, <https://doi.org/10.1016/j.biomaterials.2005.07.034>.
- [15] J.R. Kelly, I. Denry, Stabilized zirconia as a structural ceramic: an overview, *Dent. Mater.* 24 (2008) 289–298, <https://doi.org/10.1016/j.dental.2007.05.005>.
- [16] T. Liu, X.F. Zhang, L. Yuan, J.K. Yu, A review of high-temperature electrochemical sensors based on stabilized zirconia, *Solid State Ion.* 283 (2015) 91–102, <https://doi.org/10.1016/j.ssi.2015.10.012>.
- [17] A.G. Glukharev, V.G. Konakov, Synthesis and properties of zirconia-graphene composite ceramics: a brief review, *Rev. Adv. Mater. Sci.* 56 (2018) 124–138, <https://doi.org/10.1515/rams-2018-0041>.
- [18] F. Chen, D. Jin, K. Tyeb, B. Wang, Y.H. Han, S. Kim, J.M. Schoenung, Q. Shen, L. Zhang, Field assisted sintering of graphene reinforced zirconia ceramics, *Ceram. Int.* 41 (2015) 6113–6116, <https://doi.org/10.1016/j.ceramint.2014.12.147>.
- [19] A. Gallardo-López, I. Márquez-Abriel, A. Morales-Rodríguez, A. Munoz, R. Poyato, Dense graphene nanoplatelet/yttria tetragonal zirconia composites: processing, hardness and electrical conductivity, *Ceram. Int.* 43 (2017) 11743–11752, <https://doi.org/10.1016/j.ceramint.2017.06.007>.
- [20] C. López-Pernía, C. Munoz-Ferreiro, C. González-Orellana, A. Morales-Rodríguez, Á. Gallardo-López, R. Poyato, Optimizing the homogenization technique for graphene nanoplatelet/yttria tetragonal zirconia composites: influence on the microstructure and the electrical conductivity, *J. Alloys. Compd.* 767 (2018) 994–1002, <https://doi.org/10.1016/j.jallcom.2018.07.199>.
- [21] R. Poyato, J. Osuna, A. Morales-Rodríguez, Á. Gallardo-López, Electrical conduction mechanisms in graphene nanoplatelet/yttria tetragonal zirconia composites, *Ceram. Int.* 44 (2018) 14610–14616, <https://doi.org/10.1016/j.ceramint.2018.05.082>.
- [22] S. Li, Z. Xie, Y. Zhang, Y. Zhou, Enhanced toughness of zirconia ceramics with graphene platelets consolidated by spark plasma sintering, *Int. J. Appl. Ceram. Technol.* 14 (2017) 1062–1068, <https://doi.org/10.1111/ijac.12742>.
- [23] Z.E. Yin, H. Zhang, Y.R. Kang, J.M. Feng, Y.L. Li, Fabrication of graphene/zirconia nanocomposite by mixing graphite oxide and zirconia nanopowders and pressureless sintering, *Key Eng. Mater.* 512–515 (2012) 65–68, <https://doi.org/10.4028/www.scientific.net/KEM.512-515.65>.
- [24] J. Su, Y. Chen, Q. Huang, Graphene nanosheet-induced toughening of yttria-stabilized zirconia, *Appl. Phys. A Mater. Sci. Process.* 123 (2017) 1–11, <https://doi.org/10.1007/s00339-016-0613-7>.
- [25] H. Zou, Y. Zhang, L. Liu, L. Shi, W. Li, The toughening mechanism and mechanical properties of graphene-reinforced zirconia ceramics by microwave sintering, *Adv. Appl. Ceram.* 117 (2018) 420–426, <https://doi.org/10.1080/17436753.2018.1477566>.
- [26] S.M. Kwon, S.J. Lee, I.J. Shon, Enhanced properties of nanostructured ZrO₂-graphene composites rapidly sintered via high-frequency induction heating, *Ceram. Int.* 41 (2014) 835–842, <https://doi.org/10.1016/j.ceramint.2014.08.042>.
- [27] N. Obradović, F. Kern, Properties of 3Y-TZP zirconia ceramics with graphene addition obtained by spark plasma sintering, *Ceram. Int.* 44 (2018) 16931–16936, <https://doi.org/10.1016/j.ceramint.2018.06.133>.
- [28] S. Kim, F. Chen, L. Zhang, Q. Shen, J.M. Schoenung, Y.-H. Han, D. Jin, K. Tyeb, B. Wang, Field assisted sintering of graphene reinforced zirconia ceramics, *Ceram. Int.* 41 (2015) 6113–6116, <https://doi.org/10.1016/j.ceramint.2014.12.147>.
- [29] J. Liu, H. Guo, Y. Su, L. Wang, L. Wei, G. Yang, Y. Yang, K. Jiang, Spark plasma sintering of graphene platelet reinforced zirconia composites with improved mechanical performance, *Mater. Sci. Eng. A.* 688 (2017) 70–75, <https://doi.org/10.1016/j.msea.2017.01.107>.
- [30] K. Markandan, J.K. Chin, M.T.T. Tan, Enhancing electroconductivity of yttria-stabilised zirconia ceramic using graphene platelets, *Key Eng. Mater.* 690 (2016) 1–5, <https://doi.org/10.4028/www.scientific.net/KEM.690.1>.
- [31] K. Markandan, M.T.T. Tan, J. Chin, S.S. Lim, A novel synthesis route and mechanical properties of Si-O-C cured Yttria stabilised zirconia (3YSZ)-graphene composite, *Ceram. Int.* 41 (2015) 3518–3525, <https://doi.org/10.1016/j.ceramint.2014.11.008>.
- [32] Z. Zeng, Y. Liu, W. Chen, X. Li, Q. Zheng, K. Li, R. Guo, Fabrication and properties of in situ reduced graphene oxide-toughened zirconia composite ceramics, *J. Am. Ceram. Soc.* 101 (2018) 3498–3507, <https://doi.org/10.1111/jace.15483>.
- [33] I.J. Shon, J.K. Yoon, K.T. Hong, Properties and rapid sintering of a nanostructured tetragonal zirconia composites, *Met. Mater. Int.* 23 (2017) 940–947, <https://doi.org/10.1007/s12540-017-7069-y>.
- [34] B.K. Kim, J.W. Hahn, K.R. Han, Quantitative phase analysis in tetragonal-rich tetragonal/monoclinic two phase zirconia by Raman spectroscopy, *J. Mater. Sci. Lett.* 16 (1997) 669–671, <https://doi.org/10.1023/A:1018587821260>.
- [35] A. Flaureau, A. Weibel, G. Chevallier, C. Estournès, Study of the densification and grain growth mechanisms occurring during spark plasma sintering of different submicronic yttria-stabilized zirconia powders, *J. Eur. Ceram. Soc.* 41 (6) (2021) 3581–3594, <https://doi.org/10.1016/J.JEURCERAMSOC.2021.01.032>.
- [36] W.F. Brown, J.E. Srawley, Plane Strain. Crack Toughness Testing of High Strength Metallic Materials, 1966, <https://doi.org/10.1520/STP44663S>.
- [37] M.W. Pitcher, S.V. Ushakov, A. Navrotsky, B.F. Woodfield, G. Li, J. Boerio-Goates, B.M. Tissue, Energy crossovers in nanocrystalline zirconia, *J. Am. Ceram. Soc.* 88 (2005) 160–167, <https://doi.org/10.1111/j.1551-2916.2004.00031.x>.
- [38] S. Rani, M. Kumar, S. Sharma, D. Kumar, Role of graphene in structural transformation of zirconium oxide, *J. Solgel Sci. Technol.* 71 (2014) 470–476, <https://doi.org/10.1007/s10971-014-3401-x>.
- [39] C. Wulfman, et al., Interest of Raman spectroscopy for the study of dental material: the zirconia material example, *IRBM* 31 (2010) 257–262, <https://doi.org/10.1016/j.irbm.2010.10.004>.
- [40] M. Zhou, H. Bi, T. Lin, X. Lu, D. Wan, F. Huang, J. Lin, Heat transport enhancement of thermal energy storage material using graphene/ceramic composites, *Carbon* 75 (2014) 314–321, <https://doi.org/10.1016/j.carbon.2014.04.009>.
- [41] A.C. Ferrari, Raman spectroscopy of graphene and graphite: disorder, electron-phonon coupling, doping and nonadiabatic effects, *Solid State Commun.* 143 (2007) 47–57, <https://doi.org/10.1016/j.ssc.2007.03.052>.
- [42] M. Bayle, N. Reckinger, J.-R. Huntzinger, A. Felten, A. Bakaraki, P. Landois, J.-F. Colomer, L. Henrard, A.-A. Zahab, J.-L. Sauvajol, M. Paillet, Dependence of the Raman spectrum characteristics on the number of layers and stacking orientation in few-layer graphene, *Phys. Status Solidi B-Basic Solid State Phys.* 252 (2015) 2375–2379, <https://doi.org/10.1002/psb.201552204>.
- [43] L.G. Cançado, K. Takai, T. Enoki, M. Endo, Y.A. Kim, H. Mizusaki, N.L. Speziali, A. Jorio, M.A. Pimenta, Measuring the degree of stacking order in graphite by Raman spectroscopy, *Carbon* 46 (2008) 272–275, <https://doi.org/10.1016/j.carbon.2007.11.015>.
- [44] M.I. Mendelson, Average grain size in polycrystalline ceramics, *J. Am. Ceram. Soc.* 52 (1969) 443–446, <https://doi.org/10.1111/j.1151-2916.1969.tb11975.x>.
- [45] S. Rul, F. Lefèvre-Schlick, E. Capria, C. Laurent, A. Peigney, Percolation of single-walled carbon nanotubes in ceramic matrix nanocomposites, *Acta Mater.* 52 (2004) 1061–1067, <https://doi.org/10.1016/j.actamat.2003.10.038>.
- [46] M. Poorteman, M. Traianidis, G. Bister, F. Cambier, Colloidal processing, hot pressing and characterisation of electroconductive MWCNT-alumina composites with compositions near the percolation threshold, *J. Eur. Ceram. Soc.* 29 (2009) 669–675, <https://doi.org/10.1016/j.jeurceramsoc.2008.07.047>.
- [47] A. Kasperski, A. Weibel, C. Estournès, Ch. Laurent, A. Peigney, Preparation-microstructure-property relationships in double-walled carbon nanotubes/alumina composites, *Carbon* 53 (2013) 62–72, <https://doi.org/10.1016/j.carbon.2012.10.030>.
- [48] J.H. Shin, S.H. Hong, Microstructure and mechanical properties of single wall carbon nanotube reinforced yttria stabilized zirconia ceramics, *Mater. Sci. Eng. A* 556 (2012) 382–387, <https://doi.org/10.1016/j.msea.2012.07.001>.
- [49] A. Kasperski, A. Weibel, D. Alkattan, C. Estournès, Ch. Laurent, A. Peigney, Double-walled carbon nanotube/zirconia composites: preparation by spark plasma sintering, electrical conductivity and mechanical properties, *Ceram. Int.* 41 (2015) 13731–13738, <https://doi.org/10.1016/j.ceramint.2015.08.034>.
- [50] A. Morales-Rodríguez, R. Poyato, F. Gutiérrez-Mora, A. Munoz, A. Gallardo-López, The role of carbon nanotubes on the stability of tetragonal zirconia polycrystals, *Ceram. Int.* 44 (2018) 17716–17723, <https://doi.org/10.1016/j.ceramint.2018.06.238>.
- [51] S.S. Scherrer, I.L. Denry, H.W.A. Wiskott, Comparison of three fracture toughness testing techniques using a dental glass and a dental ceramic, *Dent. Mater.* 14 (1998) 246–255, [https://doi.org/10.1016/S0109-5641\(98\)00032-3](https://doi.org/10.1016/S0109-5641(98)00032-3).
- [52] G.D. Quinn, R.C. Bradt, On the Vickers indentation fracture toughness test, *J. Am. Ceram. Soc.* 90 (2007) 673–680, <https://doi.org/10.1111/j.1551-2916.2006.01482.x>.
- [53] X. Wang, N.P. Padture, H. Tanaka, Contact-damage-resistant ceramic/single-wall carbon nanotubes and ceramic/graphite composites, *Nature Mater.* 3 (2004) 539–544, <https://doi.org/10.1038/nmat1161>.
- [54] R. Poyato, A. Gallardo-Lopez, F. Gutierrez-Mora, A. Morales-Rodriguez, A. Munoz, A. Dominguez-Rodriguez, Effect of high SWNT content on the room temperature mechanical properties of fully dense 3YTZP/SWNT composites, *J. Eur. Ceram. Soc.* 34 (2014) 1571–1579, <https://doi.org/10.1016/j.jeurceramsoc.2013.12.024>.
- [55] B.W. Sheldon, W.A. Curtin, Nanoceramic composites: tough to test, *Nat. Mater.* 3 (2004) 505–506, <https://doi.org/10.1038/nmat1174>.
- [56] A. Duszova, J. Duszka, K. Tomasek, J. Morgiel, G. Blugand, J. Kuebler, Zirconia/carbon nanofiber composite, *Scripta Mater.* 58 (2008) 520–523, <https://doi.org/10.1016/j.scriptamat.2007.11.002>.
- [57] R. Cano-Crespo, Bi. M. Moshtaghion, D. Gómez-García, R. Moreno, A. Domínguez-Rodríguez, Graphene or carbon nanofiber-reinforced zirconia composites: are they really worthwhile for structural applications? *J. Eur. Ceram. Soc.* 38 (2018) 3994–4002, <https://doi.org/10.1016/j.jeurceramsoc.2018.04.045>.
- [58] A. Wang, P. Hu, X. Zhang, W. Han, G. Chen, J. Han, Accurate measurement of fracture toughness in structural ceramics, *J. Eur. Ceram. Soc.* 37 (2017) 4207–4212, <https://doi.org/10.1016/j.jeurceramsoc.2017.05.027>.
- [59] J. Cui, Z. Gong, M. Lv, P. Rao, Determination of fracture toughness of Y-TZP ceramics, *Ceram. Int.* 43 (2017) 16319–16322, <https://doi.org/10.1016/j.ceramint.2017.09.004>.
- [60] M. Mazaheri, D. Mari, Z.R. Hesabi, R. Schaller, G. Fantozzi, Multi-walled carbon nanotube/nanostructured zirconia composites: outstanding mechanical properties in a wide range of temperature, *Compos. Sci. Technol.* 71 (2011) 939–945, <https://doi.org/10.1016/j.compscitech.2011.01.017>.

- [61] P. Mohapatra, S. Rawat, N. Mahato, K. Balani, Restriction of phase transformation in carbon nanotube-reinforced yttria-stabilized zirconia, *Metall. Mater. Trans. A* 46A (2015) 2965–2974, <https://doi.org/10.1007/S11661-015-2897-1>.
- [62] J.L. Shi, B.S. Li, Z.L. Lu, X.X. Huang, Correlation between microstructure, phase transformation during fracture and the mechanical properties of Y-TZP ceramics, *J. Eur. Ceram. Soc.* 16 (1996) 795–798, [https://doi.org/10.1016/0955-2219\(95\)00192-1](https://doi.org/10.1016/0955-2219(95)00192-1).
- [63] J. Chevalier, L. Gremillard, A.V. Virkar, D.R. Clarke, The tetragonal-monoclinic transformation in zirconia: lessons learned and future trends, *J. Am. Ceram. Soc.* 92 (2009) 1901–1920, <https://doi.org/10.1111/j.1551-2916.2009.03278.x>.